THE ASTROPHYSICAL JOURNAL, 444:532–547, 1995 May 10

A SEARCH FOR "FAILED CLUSTERS" OF GALAXIES

W. H. TUCKER[1] AND H. TANANBAUM
Harvard-Smithsonian Center for Astrophysics, Cambridge, MA 02138; wtucker@cfa.harvard.edu; ht@cfa.harvard.edu
AND
R. A. REMILLARD
Massachusetts Institute of Technology, Cambridge, MA 02139; rr@space.mit.edu
Received 1994 September 12; accepted 1994 November 16

ABSTRACT

We describe a search for a new type of object—large clouds of hot gas with no visible galaxies—which we call failed clusters of galaxies. We calculate the expected X-ray luminosity, temperature, and angular diameter of such objects as a function of total cloud mass and convert the results to expected X-ray fluxes from failed clusters at different redshifts.

Using the *Einstein* Imaging Proportional Counter (IPC) database, we establish a strategy to search for candidate failed clusters. From this initial screening of 1435 IPC fields, 17 candidates are selected for more detailed analysis, which indicates that 10 of these are very probably extended X-ray sources. Optical follow-up on the 10 prime candidates finds eight clusters of galaxies (including six reported for the first time in this paper), one stellar identification, and one without an obvious optical counterpart (the candidate with the weakest evidence for X-ray extent). Investigation of several candidates with less evidence for X-ray extent yields two additional new clusters of galaxies.

A conservative comparison of our results with the *Einstein* Extended Medium Sensitivity Survey demonstrates that failed clusters are at most one-sixth as common as clusters of galaxies (98.3% confidence level). Therefore we conclude that failed clusters are a relatively unimportant contributor to the mass density of the universe. Our inability to find failed clusters is consistent with the hierarchical clustering scenario for the formation of galaxies and clusters.

Subject headings: galaxies: clusters: general — galaxies: formation — X-rays: galaxies

1. INTRODUCTION

One of the major problems affecting our understanding of the origins of galaxies and clusters of galaxies is the limited data available for generating or testing the various theories. For example, what was the efficiency of galaxy formation from primordial clouds? How does this efficiency depend on the power spectrum of the fluctuations giving rise to these structures?

Some information bearing on questions such as these has been presented in recent papers. X-ray studies of clusters of galaxies (David et al. 1990; Edge & Stewart 1991; Tsuru 1991) show that the observed ratio of gas mass to stellar mass in a cluster varies from near unity in groups and poor clusters to approximately five in rich clusters. If we define the efficiency of galaxy formation ϵ as the fraction of primordial gas in a pregalactic cloud which is consumed into stars, then

$$\epsilon = \frac{1}{(1-\beta)}\left(\frac{M_*}{M_* + M_x}\right), \quad (1)$$

where M_x is the observed mass in gas, M_* is the observed mass in stars, and β is the fraction of stellar mass that has been ejected in a galactic wind but retained as gas in the cluster. We assume that dark matter, whether baryonic or nonbaryonic, is distributed proportionately to the gaseous and stellar components. Numerical simulations by David, Forman, & Jones (1991) indicate that $\beta \approx 0.25$ provides the best fit to the elemental abundances observed for the intracluster medium. The efficiency of galaxy formation derived from X-ray observations therefore ranges from ≈ 0.7 for groups and poor clusters to ≈ 0.2 in rich clusters, assuming that groups and clusters are closed systems. Winds which ejected mass from the system, if they existed, would be more likely in groups, so the efficiency calculated for groups might be overestimated.

David & Blumenthal (1992) showed that the observed range for the efficiency of galaxy formation for groups and clusters can be readily explained in a hierarchical clustering, cold dark matter scenario. A wide range of parameters describing the power spectrum, magnitude, and mass of the primordial fluctuations yield values for ϵ consistent with both the observed magnitude of ϵ and the trend of decreasing efficiency with increasing cluster richness.

We can also estimate a globally averaged efficiency of galaxy formation, ϵ_{gl}, based on observations of large-scale structure and motions. From the observed mass to light ratio of $\sim 200\,h$ for groups and clusters (de Lapparent, Huchra, & Geller 1989) and the required mass to light ratio of $\sim 2400\,h\,\Omega$ (Marzke, Huchra, & Geller 1994) for a critical mass density, one can infer

$$\epsilon_{gl} \approx 0.08\Omega^{-1}, \quad (2)$$

where h is the Hubble constant in units of 100 km s^{-1} Mpc^{-1} and Ω is the average density in the universe normalized to the critical density needed for closure.

The observations of David et al. (1990) imply an average $\epsilon \sim 0.4$, for groups and clusters of galaxies if they are described by the Schechter-type mass function used by Bahcall & Cen (1993) to fit the masses of groups and clusters. If the luminous

[1] Also at University of California, San Diego.

matter is distributed similarly to the dark matter and $\Omega = 1$, then for $h = 0.7$ a fraction $\alpha = 0.80\ (1\text{–}2.5\ \epsilon_v)^{-1}$ of the mass of the universe must be in regions outside of groups and clusters, where the efficiency of galaxy formation is $\epsilon_v \ll 1$ in order to bring the global efficiency down to 0.08. As ϵ_v varies from 0 to 0.08, α ranges from 0.80 to 1, so most of the luminous mass must be outside groups and clusters in regions of low ϵ_v, if $\Omega = 1$. The galaxy number density in the Bootes and other voids is a factor of 10 less than the mean (Moody et al. 1987; de Lapparent, Geller, & Huchra 1991), which implies that $\epsilon_v \ll 1$ if indeed most of the mass is in the voids, as required by $\Omega = 1$. Alternatively, Einasto et al. (1994) have concluded that the mass fraction in the voids is only ≈ 0.15 (much less than the minimum value of $\alpha = 0.80$ obtained from the relationship above), which would require $\Omega < 1$ or different distributions for dark and baryonic matter (White 1991; Kang et al. 1994).

These qualitative considerations indicate that studies of the efficiency of galaxy formation relate to and potentially constrain a number of interesting questions such as: the spectrum of fluctuations that gave rise to galaxies, the baryonic or nonbaryonic nature of dark matter, the value of Ω, and the relative distribution of dark and baryonic matter.

In this paper we describe the results of a search for a particular type of object—failed clusters of galaxies—whose existence or nonexistence bears on these questions. The theory of galaxy formation requires that galaxies form from clouds of gas whose cooling time is less than the Hubble time. This implies a protogalactic mass less than about $10^{12}\ M_\odot$ (Rees & Ostriker 1977; Silk 1977; Blumenthal et al. 1984; White & Frenk 1991). Clouds more massive than $10^{12}\ M_\odot$ have a cooling time longer than a Hubble time and could in principle have never collapsed to form stars in appreciable numbers. The result would be a large cloud of gas with no visible galaxies. We call these hypothetical objects "failed clusters" of galaxies. Using scaling arguments it is possible to estimate the expected luminosity, temperature, and angular diameter of failed clusters (see § 2). These arguments imply that failed clusters with virial masses (we assume that the ratio of virial mass to gas mass $=10$) greater than $10^{14}\ M_\odot$ should be observable as X-ray sources to redshifts $z \sim 0.1$, while failed clusters with masses greater than $10^{16}\ M_\odot$ should be observable as X-ray sources to $z \sim 1.0$. Such failed clusters would have angular diameters of several arcminutes. We are searching for extreme objects in which no galaxies are detected in clouds with virial mass $\gtrsim 10^{14}\ M_\odot$. If we assume that we can detect a galaxy of magnitude $m_v \sim 20$ at redshift $z \sim 0.2$, and that the typical mass to light ratio for a galaxy $=100$, then a failure to detect at least one galaxy would imply $\epsilon \lesssim 10^{-2}$.

The number of such objects expected is already constrained by limits on the angular fluctuations in the X-ray background. For example, if it is assumed that the Bootes void has a normalized mass density Ω which is due almost entirely to failed clusters, then $\sim 600\Omega$ failed clusters of mass $10^{14}\ M_\odot$ would be required in the ~ 600 deg^2 area of void. The integrated X-ray flux over the void from this hypothetical population of failed clusters would be $\sim 4 \times 10^{-9}\ \Omega$ ergs cm^{-2} s^{-1}, corresponding to $\sim 6 \times 10^{-12}\Omega$ ergs cm^{-2} s^{-1} deg^{-2}. This projected surface brightness is a factor of $\sim 30\Omega$ greater than the limit set by the *HEAO 1* A-2 survey (Shafer 1983) on a scale of ~ 10 deg^2. Thus the *HEAO 1* A-2 data limit an Ω due to failed clusters in the void to values ≤ 0.03.

Although this X-ray background constraint indicates that failed clusters are not a significant contributor to the mass density of the universe, the existence or nonexistence of such objects is nevertheless of interest for theories of structure formation. For example, if structure formation follows a "top-down" or similar scenario with significant power density on a large scale, the possibility exists that significant numbers of failed clusters could have formed. Alternatively, if the formation of galaxies and clusters of galaxies follows a hierarchical clustering scenario starting from masses of galactic size or less (e.g., Peebles 1980) then the cooling times of the clouds would have been less than a Hubble time and no failed clusters are expected. Thus, the discovery of even one failed cluster in a survey such as ours would pose serious difficulties for any hierarchical clustering scheme.

In § 2 we invoke some simple scaling laws to describe the qualitative nature of hypothetical failed clusters. In § 3 we describe the methodology used to search the *Einstein* Imaging Proportional Counter (IPC) database for failed clusters. The X-ray analysis techniques are described in § 4, and the optical and infrared follow-up observations are described in § 5. The implications of our failure to find failed clusters, which we interpret as support for hierarchical clustering schemes, are discussed in § 6.

2. QUALITATIVE CHARACTERIZATION OF FAILED CLUSTERS

Consider a cloud of initial mass M, with a baryonic mass $M_x = f_x M$ in the form of hydrogen gas, that has condensed out of the Hubble flow and come to virial equilibrium at a redshift z_f. The cloud radius R scales as

$$R \propto M^{1/3}/(1 + z_f)\ , \tag{3}$$

and its temperature T_x scales as

$$T_x \propto M/R \propto M^{2/3}(1 + z_f)\ . \tag{4}$$

The total bremsstrahlung X-ray luminosity L_x of the cloud scales as

$$L_x \propto M_x^2 R^{-3} T_x^{1/2} \propto f_x^2 M^{4/3}(1 + z_f)^{7/2}\ . \tag{5}$$

If we assume that the gas is distributed according to an isothermal model with core radius a, then the relation of a to M and z_f involves an understanding of the evolution of the cluster gas. For the case of failed clusters, the simplest procedure is to assume that this evolution is self-similar, that is, that $a \propto R$, so the scaling relations in terms of the core radius are the same as given by equations (3), (4), and (5) (Henry et al. 1992).

Although the Coma cluster is not a failed cluster, over 80% of its luminous matter is in the form of hot gas, so we should be able to obtain a rough estimate of the luminosity and size of failed clusters by normalizing to the Coma cluster. Taking the emission measure and temperature determined by Hughes et al. (1993), and the total mass within $1.5\ h^{-1}$ Mpc from Hughes (1989), assuming that the luminosity of a failed cluster with the mass of Coma is $\sim 35\%$ larger than Coma because $\sim 14\%$ of the baryonic mass of Coma is locked up in stars, and assuming that all clusters were formed at the same redshift, then for $h = 0.7$ we predict values for the present luminosity, temperature, and core radius:

$$L = (1.4)10^{45} M_{15}^{4/3}\ \text{ergs s}^{-1} \quad (\propto h^{7/3})\ , \tag{6}$$

$$T = 8.4 M_{15}^{2/3}\ \text{keV} \quad (\propto h^{2/3})\ , \tag{7}$$

$$a = 0.31 M_{15}^{1/3}\ \text{Mpc} \quad (\propto h^{-2/3})\ , \tag{8}$$

where M_{15} is the mass inside 2 Mpc (~ 7 core radii) in units of $10^{15}\,M_\odot$.

The cooling time t_c of the X-ray–emitting gas inside the core radius is (assuming $f_x = 0.1$):

$$t_c = 3kT/n\Lambda = 10^{10.3} M_{15}^{1/3}\ \mathrm{yr} \quad (\propto h^{-5/3})\,, \tag{9}$$

where Λ is the radiative cooling coefficient for a gas of number density n with cosmic abundances of hydrogen and helium and no heavier elements. For $M_{15} > 0.1$, the present cooling times are greater than 10^{10} yr, or the approximate age of the clouds; for clusters formed at $z_f < 2$, this limit on the mass ensures that the cooling time of the clouds has always been less than their age. In principle, the clouds could have remained hot since their formation.

The fraction $(\Delta L/L)$ of the total radiative flux from the cluster gas which falls in the *Einstein* IPC band depends on the present redshift and temperature of the cluster. Taking an effective band width of 0.8 to 3.5 keV, and a constant Gaunt factor, we obtain

$$(\Delta L/L) = e^{-0.8(1+z)/T}(1 - e^{-2.7(1+z)/T})\,. \tag{10}$$

For a typical cloud with $T = 7$ keV and $z = 0.2$, $\Delta L/L$ for the 0.8–3.5 keV band has a value of about one-third, which is 75% of its value for the 0.3–3.5 keV band used in the Extended Medium Sensitivity Survey (EMSS; Gioia et al. 1990).

Using equations (6), (7), (8), and (10), we calculate the flux in the X-ray band and the angular diameter of the core radius as functions of the mass and redshift of the failed cluster. In Figure 1 we show curves corresponding to failed cluster X-ray fluxes of 10^{-11}, 10^{-12}, and 10^{-13} ergs cm^{-2} s^{-1} in the 0.8 to 3.5 keV band as a function of total mass and redshift.

Figure 1 shows that failed clusters with masses ranging from 10^{14} to $10^{16}\,M_\odot$ should be detectable at redshifts ranging from $z = 0.1$ to 1 at a level of 10^{-12} ergs cm^{-2} s^{-1}, which is the level of sensitivity reached or exceeded by 90% of the EMSS. The angular size of the core diameters for these objects would be $\approx 7\ M_{15}^{1/3}$ arcmin at $z = 0.1$, and $\approx 2M_{15}^{1/3}$ arcmin at $z = 1$. Indeed, normal clusters with similar parameters were detected in the EMSS with a surface density of approximately 1 per 10 deg^2. In our survey we consider sources close to ribs and edges of the IPC, which raises the area to almost 1 deg^2 for each IPC field or $\sim$twice the area available to EMSS. This increase is offset somewhat by the narrower bandwidth, which reduces the depth to which we search by approximately 25%. We estimate that if the ratio of failed clusters to normal clusters is $f_{\rm fc}$, then we might expect to find $\sim 100 f_{\rm fc}$ failed clusters in the IPC database. (See § 6 for a somewhat refined estimate which includes the efficiency of our process for selecting failed cluster candidates.)

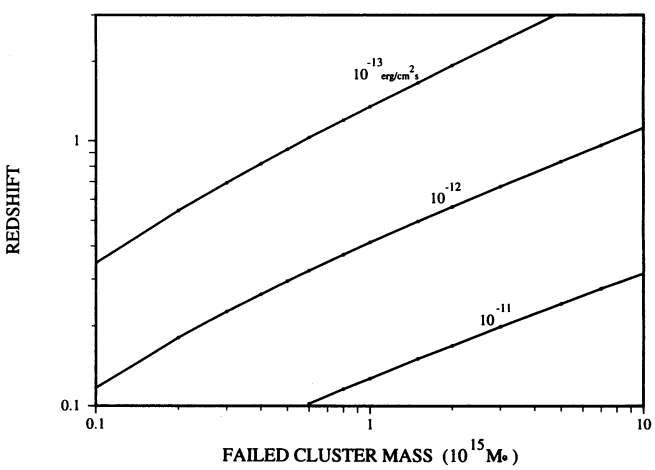

FIG. 1.—Predicted X-ray flux (0.8–3.5 keV) for failed clusters as a function of redshift and failed cluster mass (in units of $10^{15}\,M_\odot$). The solid lines correspond to X-ray fluxes of 10^{-11}, 10^{-12}, and 10^{-13} ergs cm^{-2} s^{-1}.

3. METHODOLOGY OF SEARCHING IPC DATABASE FOR FAILED CLUSTERS

Our strategy for searching for failed clusters in the IPC database involved the following steps: (1) look only at fields with absolute value of galactic latitude $|b| > 20°$ and exposure time ≥ 800 s; (2) exclude fields containing a large, known extended source, such as a supernova remnant, a nearby galaxy or cluster of galaxies, a star cluster, or a bright X-ray source (≥ 0.6 counts s^{-1}); (3) accept only objects with signal/noise ratio ≥ 3; (4) keep only sources for which the parameter SIZCOR in the *Einstein* Catalog (Harris et al. 1993) is ≥ 1.5; SIZCOR is defined as the ratio of the intensity contained within the 3 σ contour to the intensity within the 2.4 × 2.4 detection box; this is a preliminary criterion for finding candidate extended X-ray sources: 39 of 95 X-ray selected clusters in the EMSS survey have SIZCOR ≥ 1.5; and (5) exclude objects identified in the *Einstein* Catalog with a known radio, infrared, or optical counterpart.

Criteria (1) and (2) are the same as for the EMSS. We do not employ the following additional EMSS criteria for the reason given in parentheses: (1) all three detection algorithms (LDETECT, XDETECT, and MDETECT, Harnden et al. 1984, hereafter H84) are required to detect the source (we did not require a detection by MDETECT because MDETECT can miss extended sources); and (2) regions in which one or more of the central nine detection subcells (each subcell is 48″ × 48″) are shadowed by the window-supporting ribs of the IPC or the edge of the detector field of view are excluded (we developed techniques which are less sensitive to these obscuring effects; § 4). Our third criterion requires only a 3 σ detection, while the EMSS requires 4 σ (we are looking for new and perhaps rare objects so that we can afford to be more speculative with regard to source existence).

We screened the 1435 IPC fields that satisfied conditions (1) and (2) above, and we applied criteria (3), (4), and (5) to the sources in these fields. Twenty-two X-ray sources emerged from this process. We found three additional sources in the IPC X-ray maps which appeared extended but had no SIZCOR information available because they were not listed in the *Einstein* Catalog (Harris et al. 1993). Since the contour maps were very suggestive, we retained these objects in our sample for further analysis. We then used the NASA Extragalactic Database and various catalogs to search for further identifications. This step eliminated eight of our X-ray sources (comprised of three identified EMSS sources—two clusters and one AGN—simply missed by us in our first pass through the data, two Southern Abell clusters, one compact group of galaxies, one QSO, and one galaxy which may be a BL Lac object). As a result, we were left with 17 prime failed cluster candidates for further X-ray analysis and optical observations.

We note that none of these 17 prime candidates was found in the 27 IPC sequences which lie in the Bootes void and meet our search criteria. At the distance of the Bootes void, we should have been able to detect failed clusters with $M \gtrsim 10^{14}\,M_\odot$. We discuss the significance of this null result in § 6.

4. X-RAY ANALYSIS OF CANDIDATE SOURCES

For the 17 candidate failed cluster sources with SIZCOR ≥ 1.5 and no optical counterpart found in our catalog and NED searches, we require a more careful analysis for possible X-ray extent. Appendix A describes how we utilize *Einstein* observations of a known point source, LMC X-1, to compute R3, the ratio of source counts in a circle (0–60)″ to source counts in an annulus (60–160)″, and to characterize the expected values of R3 for point and extended sources. For the relatively faint X-ray sources comprising our list of failed cluster candidates, we must take great care in subtracting background and in determining the position at which to center the circle and annulus.

As explained in Appendix A we selected pulse channels 5–12 for our analysis in order to maximize the signal-to-noise for source detection and extent analysis, while minimizing the variation in point response function with pulse height. This choice of pulse height channels corresponds to an energy range from ~ 0.8 to ~ 5.8 keV for an average detector gain in the middle of the *Einstein* range (BAL $\sim$ 15; see Appendix A for further details). Use of pulse height data precluded our utilization of the "standard" *Einstein* pulse invariant (PI) bins with global background maps. Therefore, we performed background subtraction by selecting a 300″ radius circle, away from known or potential sources via a visual examination of each IPC image. The background region was chosen to lie at approximately the same distance (in both linear coordinates) from the IPC center as the candidate source. When necessary, we slightly adjusted the location of the background circle so that it totally fit inside the IPC window support structure (ribs) or totally between the ribs and the edge of the field of view. In a few cases, multiple choices for the background region were evaluated to ensure that we did not oversubtract the background, leading to negative net source counts.

Our technique for determining the X-ray source location depended on the source intensity. For sources with more than 50 counts, the source positions provided by the *Einstein* Catalog (Harris et al. 1993) provided good initial estimates, which we updated based on the peak of the R3 ratio and/or the peak in the number of X-rays within an 80″ radius. For sequences 5803, 6318, 7028, and 10227, with the source near the edge of the field of view, we unmasked the IPC image (using newly available software and image files) and updated the source position by again finding the location which maximized the number of counts in an 80″ radius circle. This approach was clearly biased toward centering on pointlike sources or source regions and therefore was relatively conservative with regard to assessing source extent.

For sources with fewer than 50 counts, we determined the best position starting from the *Einstein* Catalog location (or visual estimate when the source was not listed in the catalog). We measured the number of counts contained in an 80″ radius circle, and then moved the circle around the source position measuring the counts within the circle at each step. To smooth over effects due to pixel-to-pixel counting fluctuations, we took all circles having counts within a few of the maximum and computed an unweighted centroid for these locations as our best estimate for the source position. In general, the positions changed by $\lesssim 50''$ from the catalog location, comparable to the 1 σ uncertainties in the catalog positions. In one instance, seq. 6339, the position moved by $\sim 1'.2$, probably due to the very small number of detected photons. Interestingly, the original catalog position for this source is within $\sim 0'.6$ of an $m_v = 14.5$ DA white dwarf which is a likely optical counterpart, while the revised (but somewhat uncertain) X-ray position is $1'.6$ from the white dwarf. Since positions given in this paper generally differ slightly from the *Einstein* Catalog positions, we use the IPC sequence numbers rather than coordinate names to specify sources.

We next computed an average value for R3 over a 3×3 pixel (1 pixel $= 8''$) region centered on the "best" position effectively smoothing the data to use in assessing possible source extent. In our later calculations of probability of extent, we were careful to use the counts appropriate for a single measurement of R3 (since the data points are not independent) to estimate the uncertainty in the average R3.

As stated above, for seq. 5803, 6318, 7028, and 10227 with the source located very near the edge of the field of view, we unmasked the image to ensure that we collected all of the source counts for an accurate determination of R3 and other source properties. Several other cases of nonzero RECO (rib and edge code) involved partial obscuration caused by the ribs, requiring a careful case-by-case examination. At times rib obscuration will remove counts from both the inner circle and the outer annulus with lesser impact on the ratio of the two (R3). In other cases, obscuration by the ribs will affect only the outer annulus, thereby increasing the computed value of R3 which may result in the rejection of a possibly extended source but which will not erroneously make a point source look extended. For three of our candidate failed clusters (seq. 6339, 10152, and 0435) examination of the images indicated that elimination of the most heavily obscured quadrant would provide a more reliable estimate for source extent and source flux, so we used only the data from the remaining three quadrants to compute R3.

Table 1 provides a summary for the 17 candidate failed cluster sources. Column (1) gives our best estimate (B1950 coordinates) for the X-ray source location using the procedures described above. Column (2) gives the *Einstein* IPC sequence number and when available the *Einstein* Catalog Source number for each candidate. Column (3) provides the net source counts found in pulse height channels 5–12 in a circle of radius 160″ around each source position. A crude conversion from X-ray counts to flux using equation (11) is also provided in column (3) scaling from the net counts within the 160″ circle:

$$\text{Flux} = \frac{\text{Net Counts}}{\text{Live Time}} \frac{1}{\text{Vignetting}} 4 \times 10^{-11} \text{ ergs cm}^{-2} \text{ s}^{-1} . \quad (11)$$

The vignetting value is determined for the appropriate distance off-axis using the formulae given by H84. We use a conversion factor from counts per second to ergs cm^{-2} s^{-1} for the hard PI (pulse height invariant) band corresponding to energies 0.8–3.5 keV (which would correspond to pulse height channels 5–10 for an average gain, BAL = 15). H84 quote 3.45×10^{-11} as the factor to use in converting hard-band counts to flux (for an assumed power-law spectrum with photon index $= 1.5$ and hydrogen column density 2×10^{20}). We multiply this constant by a factor of 1.16 (midway between 1.14 and 1.18; see H84) to account for mirror scattering of photons outside our 160″ collection circle. The product provides the factor of 4.0×10^{-11} given in equation (11). Note that these estimates do not take into account possible source extent (photons falling outside the 160″ radius circle), which would increase the fluxes nor do they

TABLE 1

EINSTEIN IPC CANDIDATE FAILED CLUSTER CANDIDATES

X-Ray Position (B1950) (1)	IPC Sequence no., EOSCAT Source no. (2)	X-Ray Counts X-Ray Flux (10^{-13} ergs cm^{-2} s^{-1}) (3)	X-Ray Extent (4)	100 μm Source (5)	Optical (6)
$02^h07^m04^s.0$, 02°08′51″	3978	24	Indeterminate	...	Cluster
	536	3.4			
02 16 5.9, 14 23 55	6339	6.3*(4/3)	Indeterminate	...	Star?
	555	1.0			
03 25 52.7, −21 50 52	7028	63	Yes	Yes	Cluster
	780	4.9			
03 44 37.2, −01 00 28	3178	13	Yes	Cirrus	Star
	N/A	6.1			
06 57 31.1, −55 52 59	9961	304	Yes	Yes	Cluster
	1759	65			
08 06 10.3, 20 33 31	3835	75	Possible	Cirrus	NED and CTIO
	1923	6.2	extent		negative
08 39 46.0, −03 38 24	10227	55	Indeterminate	...	NED
	2037	15			negative
10 16 17.7, −07 34 31″.2.....	6098	41	Indeterminate	...	NED
	2256	2.2			negative
11 50 2.9, 03 45 38	7107	82	Yes	Yes?	Cluster
	2554	6.6			
12 18 24.1, 69 21 53	5803	206	Yes	Yes	Cluster
	2667	14			
14 45 36.0, 63 06 14	6318	21	Indeterminate	...	NED
	3334	3.2			negative
15 28 0.2, 70 06 51	6896	110	Yes	No	Cluster
	3442	11			
16 15 9.1, 33 05 52	6319	14	Indeterminate	...	Cluster
	3633	2.8			
16 46 32.0, 82 38 26	1910	158	Yes	Yes	Cluster
	3765	4.5			
17 02 33.5, −01 43 26	10152	24*(4/3)	Indeterminate	...	Star
	3819	18			
17 03 52.5, −01 28 06	10152	132	Yes	Cirrus	Cluster
	N/A	35			
23 07 55.0, −44 03 43	0435	40*(4/3)	Yes	No	Cluster
	4689	17			

NOTES.—*0207+02*: Despite the indeterminate status of X-ray extent, a rich and distant cluster was observed in our *I*-band image (Fig. 8). Fifty-five galaxies were counted within 1′.5 of the X-ray position, with only the brightest few of these visible in the Palomar "E" print.

0216+14: X-ray position shifted ∼1′.2 from *Einstein* Catalog position based on search for X-ray peak. Shadowing by IPC ribs produced small, but discernible effect on estimate for X-ray extent, so most heavily shadowed quadrant excluded, and remaining $\frac{3}{4}$ of data used to evaluate extent and (scaled by 4/3) to calculate X-ray flux. Likely optical identification with $m_v = 14.5$ white dwarf, 1′.6 from position in this table and 0′.6 from original *Einstein* Catalog position.

0325−21: Near edge of field, so unmasked IPC image used to extract full complement of X-ray counts for estimate of extent and flux. Cluster ID based on subsequent NED search, listing ESO cluster at this location.

0344−01: See § 5 for discussion of ID with galactic star.

0657−55: *HEAO 1* source excluded from EMSS based on being target of observation. Cluster ID based on optical observations by A. Dressler (1992, private communication), which also show a large gravitational arc (Tucker et al. 1994).

0806+20: Observation of Jupiter so field excluded from EMSS. Single remaining, prime failed cluster candidate, see § 5 for discussion.

0839−03: Near edge of field, so unmasked IPC image used to extract full complement of X-ray counts for estimate of extent and flux.

1150+03: Observation of Saturn so field excluded from EMSS. Minimal (but nonzero) shadowing by IPC ribs, which did not affect estimate of source extent, so all of data used for analysis. Cluster ID based on subsequent NED search uncovering reference to work of Batuski et al. (1991). *IRAS* exposure is relatively low, and detection at 100 μm is probable (2.8 σ, broad peak), but not definite.

1218+69: Near edge of field, so unmasked IPC image used to extract full complement of X-ray counts for estimate of extent and flux. Included in Ultra-Soft Survey and identified as H II region galaxy ($m_v = 17.7$, $z = 0.11$) by Puchnarewicz et al. (1992), with note that "many other galaxies can be seen in the field." Cluster ID based on our *R*-band observation shown in Fig. 3, which reveals ∼40 galaxies within 2′ of the X-ray position. The H II galaxy is a ringed spiral which might signify a galaxy merger; it is notably offset to the west of the cluster center.

1528+70: Excluded from EMSS on basis of Abell cluster as target of observation. Cluster ID based on our *R*-band observation shown in Fig. 4, with more than 50 galaxies visible within 4′ of the X-ray position, over a 4 mag range in brightness. The large galaxy just WSW of the X-ray position would appear to be a central dominant type except for the surprising brightness of its neighbor to the WNW. This configuration could be either a binary cluster or a central-dominant cluster with a foreground galaxy. Redshift measurements of the two brightest galaxies plus several fainter ones would be highly desirable.

1615+33: Evidence for X-ray extent indeterminate; cluster ID based on our *R*-band observation shown in Fig. 9. Galaxy marked "A" in Fig. 9 appears to be central dominant member of a cluster with 39 galaxies within 2–3 mag and 2′ of "A." There may be many more galaxies within 4 mag of Galaxy A. Only "A" is visible on the Palomar finding chart. The diameter of "A" is $\gtrsim 7''.1$. If we assume that this diameter is ∼75 kpc, then the cluster redshift is ∼0.45.

1646+82: Minimal (but nonzero) shadowing by IPC ribs, which did not affect estimates of source extent, so all of data used for analysis. Rich cluster ID based on our follow-up optical observation shown in Fig. 5. We count 90 galaxies within 3′ of the X-ray position, all within 3 mag of the brightest three galaxies. There is no central dominant member here; the three brightest galaxies are within ∼1′ of the cluster center, and the one with the most extended halo is not the brightest.

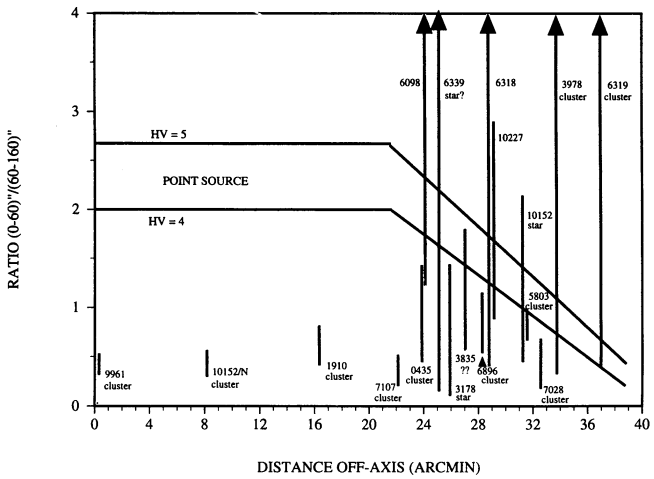

FIG. 2.—Ratio R3 [IPC counts from (0-60)" divided by IPC counts from (60–160)"] for failed cluster candidates plotted as a function of source distance (in arcmin) from the axis of the *Einstein* telescope. Vertical lines show the 90% confidence region for R3, with each candidate failed cluster labeled by its corresponding IPC sequence number (see Table 1). Candidates subsequently identified or tentatively identified are so labeled beneath the IPC seq. number. Upward pointing arrows for five sources indicate that the upper end of the 90% confidence region lies above the upper boundary of the figure. The region labelled "POINT SOURCE" between the pair of horizontal and then downward sloping lines corresponds to values of R3 expected for point sources (see text for further details). Extended X-ray sources should have values of R3 lying below the HV = 4 curve.

take into account actual spectral parameters or precise gain for a given observation. Hence, our characterization as a "crude" conversion from X-ray counts to flux.

The results of our analysis for possible X-ray extent are shown in Figure 2 and summarized in column (4) of Table 1. Figure 2 shows the value of R3 for each of the 17 candidates (labeled by IPC sequence number) plotted as a function of source distance off-axis. Each data point represents the 90% confidence interval for R3 as determined by a maximum likelihood routine which utilizes the Poisson statistics associated with the total counts (0–60)", total counts (60–160)" and background counts (300" radius circle) scaled to the two source regions. For relatively high source rates the errors are symmetric and agree with those determined by Gaussian combinations of $N^{1/2}$ uncertainties, but for low counting rates the error bar to the high side of the nominal ratio is substantially larger than the error bar to the low side. By choosing 90% confidence regions, we roughly expect to err in our assessment that a source is extended no more than once for ~ 10 sources having an upper boundary for their R3 confidence region near but still below the region associated with point sources. The two pairs of straight lines in Figure 2 are those from Figure 12 for the LMC X-1 point source calibrations with high voltage values HV = 4 and HV = 5. (See Appendix A; also note that Fig. 12 shows 3 or 4 of the 26 calibration points falling below the nominal point source region, suggesting we should interpret the evidence for extent based on 90% confidence regions with some caution.)

For nine of the 17 candidate sources the 90% confidence region for R3 lies below the line for HV = 4 and therefore outside the point source regime. These nine objects are labeled "Yes" under X-ray Extent in Table 1. A tenth source (seq. 3835) has the 90% confidence region reaching into the point source domain and therefore is labeled with Possible extent in Table 1. In principle the other seven candidate sources could be either pointlike or extended as seen by the IPC; they are labeled Indeterminate in Table 1.

5. OPTICAL AND INFRARED OBSERVATIONS

In our search for possible failed clusters, we pursued optical and IR identifications giving highest priority to the nine candidates which are probably extended and the tenth which is possibly extended. For these 10 prime candidate sources, IPAC provided summed *IRAS* data (100 μm co-added scans) as indicated in column (5) of Table 1. For three of the sources, the presence of cirrus rendered the information on the target not usable. For the other seven sources (all identified below as clusters), the *IRAS* data indicated the presence of a 100 μm source for all but seq. 0435 and 6896.

Follow-up catalog searches and new optical observations have produced cluster identifications for eight of the X-ray extended candidates: seq. 7028 (ESO cluster found in subsequent NED search); seq. 9961 (optical observations by Dressler 1992); seq. 7107 (poor cluster discovered by Batuski et al. 1991 with reference found in subsequent NED search); seq. 10152 (optical observations by Barlow & Junkarinen 1992); and seq. 5803, 6896, 1910, and 0435 (clusters discovered via our CCD observations).

Our imaging observations of failed cluster candidates were obtained using the facilities of both the Michigan-Dartmouth-MIT (MDM) Observatory and Cerro Tololo Interamerican Observatory (CTIO). The MDM observations were made with the 2.4 m Hiltner telescope in the *R* band with a 2048 pixel CCD operated with an angular scale of 0".24 per pixel. CTIO observations were conducted with both the 1.5 and 0.9 m telescopes, using the Tek 2048 and TI no. 3 CCDs along with their broad-band filter sets. The pixel scales were 0".4 and 0".31 pixel^{-1}, respectively. Image processing analysis, implemented with IRAF, included standard techniques for electronic bias

NOTES TO TABLE 1—*Continued*

1702−01: Shadowing by IPC ribs produced small, but discernable effect on estimate for source extent, so most heavily shadowed quadrant excluded and remaining $\frac{3}{4}$ of data used to evaluate extent and (scaled by 4/3) to calculate X-ray flux. SIMBAD search yields likely identification as star SAO 141509 (m_v = 9.7, type KO) located ~ 26" from X-ray position.

1703−01: *HEAO 1* source excluded from EMSS based on being target of observation. Bright source excluded from *Einstein* Catalog because of failure of LDETECT to find source, presumably due to low surface brightness without a pronounced central peak; listed in Appendix G of *Einstein* Catalog as Missed Source. Cluster ID based on optical observations by T. Barlow and V. Junkarinen (1992, private communication).

2307−44: Shadowing by IPC ribs produced small, but discernable effect on estimate for source extent, so most heavily shadowed quadrant excluded and remaining $\frac{3}{4}$ of data used to evaluate extent and (scaled by 4/3) to calculate X-ray flux. High voltage changed during observation so only data obtained at step 8 (89% of live time) used in analysis. *ROSAT* X-ray observation consistent with point source (see text). Our optical observations (see Figs. 6 and 7 and text) indicate a cluster of galaxies with a central, dominant member.

subtraction and image normalization using "sky flats" obtained during twilight. Multiple exposures were obtained for each target to permit image averaging with statistical filtering to eliminate cosmic-ray events. Finally, selected photometric standards from Landolt (1992) were observed to enable conversion of the results to standard magnitudes. Figures 3–6, 8, and 9 show our CCD images with the figure captions and notes on individual sources following Table 1 summarizing our results.

Three of the prime X-ray extended candidates (seq. 0435, 3178, and 3835) did not have straightforward interpretations (e.g., as clusters of galaxies). Since they form the gleanings of our "statistical" sample, we discuss each briefly below.

The case of seq. 0435 is somewhat perplexing. A *ROSAT* PSPC observation of this object was carried out in 1993 October. The source was detected with ~ 1300 net counts (0.1–2.4 keV) in ~ 3700 s of live time. The distribution of source counts in the *ROSAT* B channel (~ 0.5 to ~ 2 keV) was essentially indistinguishable from the 1 keV on-axis point spread function published by Hasinger et al. (1992). The *ROSAT* A channel (~ 0.1 to ~ 0.4 keV) contained slightly more than one-half of the net source counts, and these soft photons were only slightly more widely distributed than the 0.19 and 0.28 keV on-axis point spread functions of Hasinger et al. (1992). The relatively soft distribution of X-rays, which is also seen in the *Einstein* data, could have produced a relatively low value of R3 for the *Einstein* IPC data and thereby led us to classify erroneously the source as extended. On the other hand, the evidence for extent in the *Einstein* data is relatively high, persisting at the 95% confidence level and failing only at the 99% confidence level.

Moreover, our *I*-band (CCD) optical follow-up with the CTIO 0.9 m telescope on 1994 January 16, provided as Figure 6, shows a cluster of galaxies containing a central, dominant galaxy of type D. We count 47 other galaxies within 3.2 of the central galaxy and within 4 mag of its brightness. A *V*-band image gives a *V* magnitude of 16.06 ± 0.05 for the central galaxy, yielding an absolute magnitude $M_v = -21.9$ (for $z = 0.0886$—see below—and $h = 0.7$, $\Omega = 1$). The *I*-band image shows an extended halo for the central galaxy, with an angular diameter of at least 40″, implying a typical galaxy diameter of ~ 75 kpc.

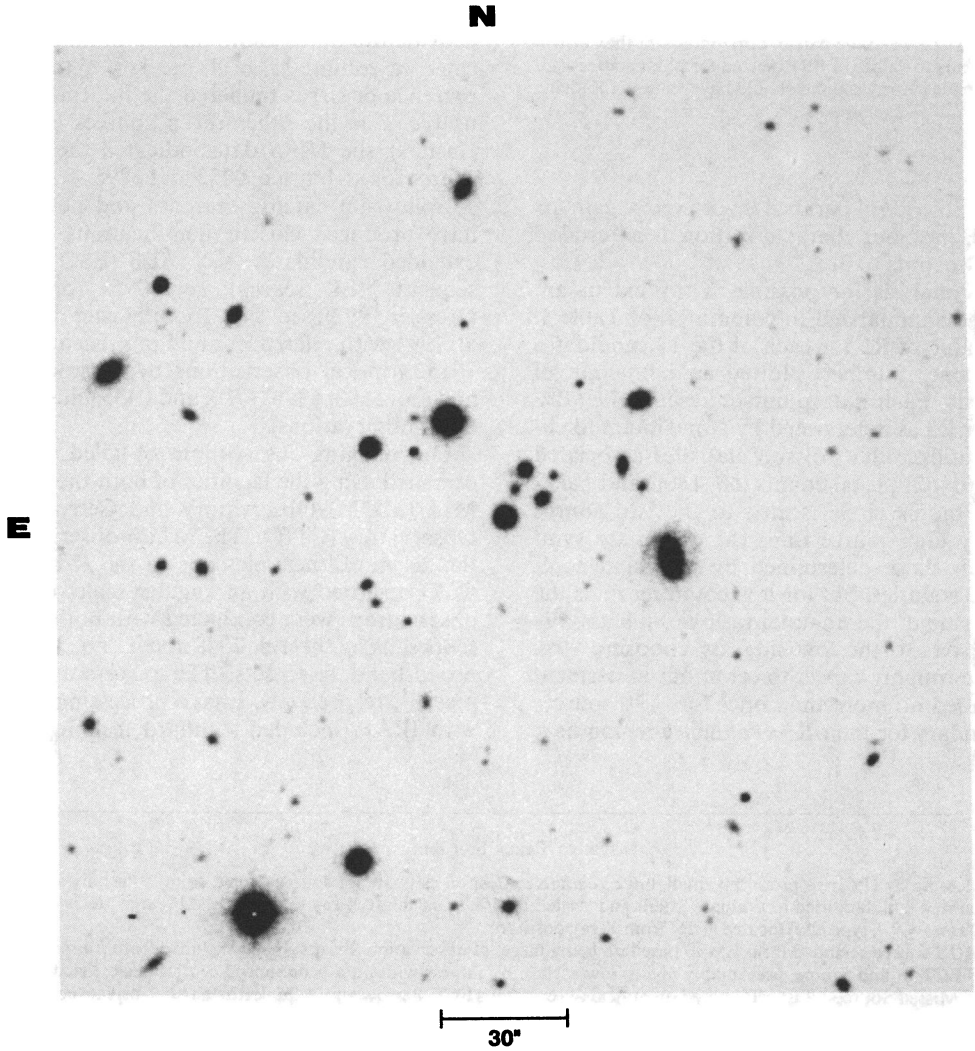

FIG. 3.—*R*-band image of 1218+69 obtained with the 2.4 m telescope at MDM Observatory. The X-ray position is ~20″ ENE of the ringed spiral to the west of the picture center. We count 40 galaxies within 2′ of the X-ray position.

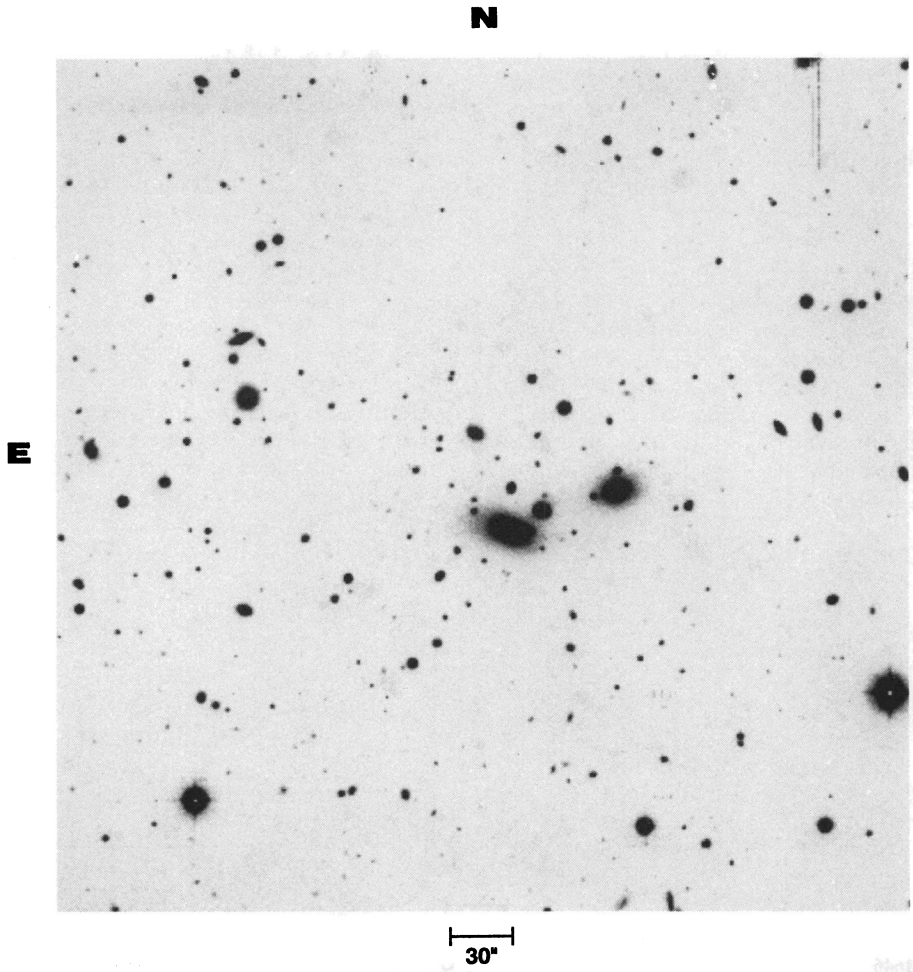

FIG. 4.—*R*-band image of 1528+70 obtained with the 2.4 m telescope at MDM Observatory. The X-ray position is 27″ ENE of the largest galaxy in the image. We count 50 galaxies within 4′ and 4 mag of the brightest galaxy, which has an impressive, extended neighbor to the WNW. This cluster may be a binary cluster containing two extended D galaxies with a projected separation less than the cluster core radius.

The *ROSAT* X-ray position [R.A. (1950) = $23^h07^m53^s.8$, Decl. (1950) = 44°03′55″.9] is ~7″ south of our measured position for the bright central galaxy. To further probe the nature of this object, optical spectra were obtained with the CTIO 4 m telescope on 1994 July 4, using the Cassegrain Spectrograph with the Tek 1024 CCD and KPGL-3 grating. The spectrum of the central galaxy (marked "A" in Fig. 6) is shown in Figure 7. All of the spectral features are absorption lines consistent (with) a stellar distribution dominated by G and K stars with a redshift of 0.0886 ± 0.0003. Galaxy "B" (see Fig. 6) was also measured through the spectrograph slit, and we observed absorption lines with a redshift of 0.0861 ± 0.0004. There is no evidence of any active nucleus, such as excess blue continuum or emission lines from H or [O III], for either Galaxy A or B.

These optical data are consistent with the X-ray extent observed in the *Einstein* data and support the identification of seq. 0435 with a cluster of galaxies, while the *ROSAT* results show an X-ray surface brightness strongly concentrated at the position of the central Galaxy. The observed *Einstein* X-ray flux and our measured redshift can be used to estimate an X-ray luminosity (0.8–3.5 keV) of $\sim 3 \times 10^{43}$ ergs s^{-1} ($h = 0.7$, $\Omega = 1$), comparable to the X-ray emission observed for many X-ray–selected clusters of galaxies. Additional analysis of the *ROSAT* spectrum and angular extent is in process, as is a check for possible variability between the *Einstein* and *ROSAT* observations. Whatever the final resolution may be, the presence of a cluster of galaxies in the CCD data indicates that 0435 is not a failed cluster.

For seq. 3178, imaging observations in the *V* and *R* bands with the 1.5 m telescope at CTIO on 1994 January 17 revealed no evidence for a cluster of galaxies, with upper limits for individual galaxies estimated at $R \sim 20.5$. Moreover, a relatively bright star ($m_v \approx 12$) lies within ~30″ of the IPC X-ray position. A spectrum of this star was obtained with the CTIO 4 m telescope in the same manner as described above. The results show absorption lines from a ~K3 star with an equivalent *V* magnitude of 12.4 (±0.2). An estimate of $\log [f_{\text{x-ray}}/f_{\text{optical}}] \approx -1.5$ to -2 for the X-ray source and the star is consistent with the K3 stellar type on the basis of the EMSS data in Table 1 of Stocke et al. (1991), so we accept the validity of this identification. It is possible that a very soft *Einstein* spectrum reduces the value of R3, thereby affecting the assessment of source extent, which does fail at the 95% confidence level.

For seq. 3835, imaging observations in the *V* and *R* bands with the 1.5 m CTIO telescope on 1994 January 17 revealed no evidence for a cluster of galaxies, with upper limits for individual galaxies estimated at $R \sim 20.5$. We note that the evidence for X-ray extent is only "possible" for this source, being mar-

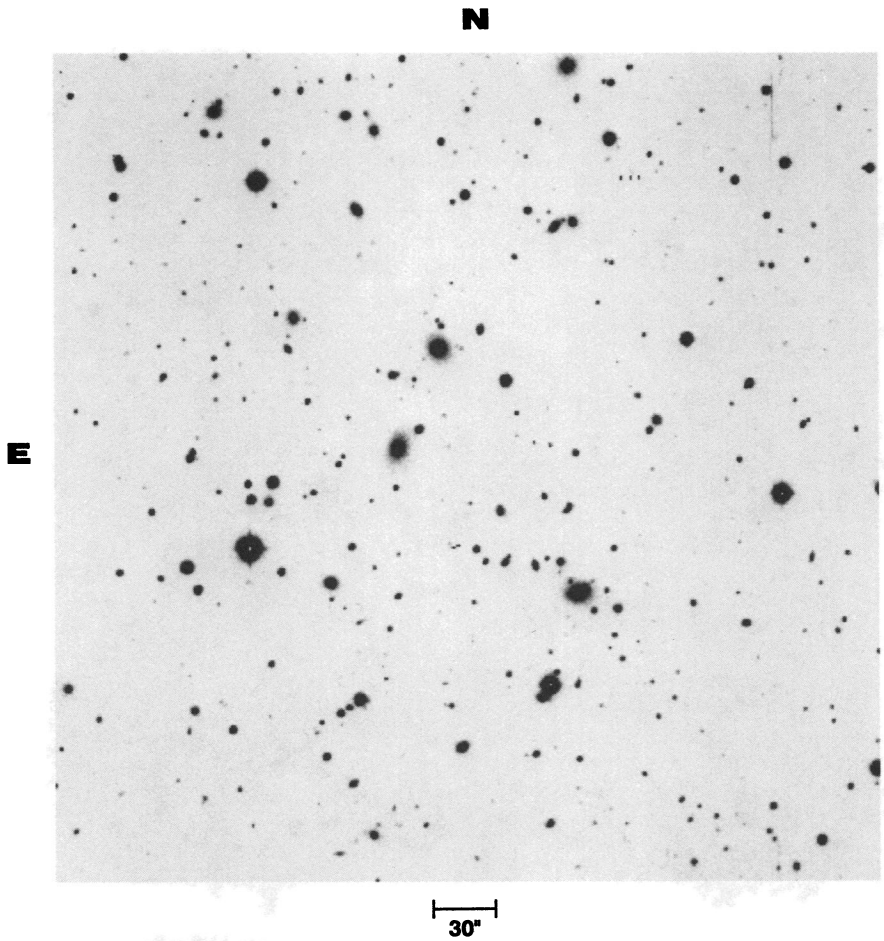

FIG. 5.—*R*-band image of 1646+82 obtained with the 2.4 m telescope at MDM Observatory. The X-ray position is ~2.5 WNW of the bright star that is ESE of the picture center. Within 3′ of the X-ray position, we count 90 galaxies interspersed with foreground field stars. The brightest three galaxies are each about 1′ from the X-ray position, and there is no central, dominant galaxy in this cluster.

ginal at the 90% level, but for now we retain it as our prime remaining candidate failed cluster.

Our decision to emphasize the 10 extended objects as our sample for optical follow-up is supported by our subsequent mixed findings for four of the seven sources characterized as having indeterminate X-ray extent. We identify seq. 10152 (1702−01) with an $m_v = 9.7$, K0 star (SAO 141509), and we have a probable identification of seq. 6339, with the $m_v = 14.5$, DA white dwarf mentioned earlier. At the same time, we identify seqs. 3978 and 6319 with previously unreported clusters of galaxies for which our CCD images are shown in Figures 8 and 9, respectively. Relevant details for these two clusters are also summarized in the figure captions and in the notes to Table 1.

6. DISCUSSION AND CONCLUSIONS

We considered the possibility that additional failed clusters could be found among the remaining unidentified sources in the *Einstein* Extended Medium Sensitivity Survey (EMSS). We took the unidentified sources listed in Table 4 of Stocke et al. (1991) and applied our criteria (particularly SIZCOR $\geq$ 1.5) to determine whether any were failed cluster candidates. Since Stocke et al. had speculated that the majority of unidentified EMSS sources might be distant clusters of galaxies and since most clusters with redshifts $\geq$0.2 are unlikely to appear extended in the IPC, we did not expect to find many X-ray extended objects (and therefore viable failed cluster candidates) among the unidentified sources. Such was the outcome of our check, with only one source—seq. 7030/source no. 944—meeting our criteria (SIZCOR = 1.6). However, the 90% confidence interval on R3 for this source ranges from 0.81 to 4.66; we therefore classified the extent as "Indeterminate" and did not pursue the object any further.

Summarizing our search for failed clusters, we have eliminated all but one primary candidate: seq. 3835 for which the evidence of X-ray extent is marginal. Conservatively, retaining this object in our failed cluster sample, we note that the probability of there actually being six failed clusters when one (or fewer) are "detected" is only 1.7%. Therefore, we set six as the upper limit in our computations comparing clusters and failed clusters.

As mentioned in § 3, we also used the EMSS cluster sample (Henry et al. 1992) to check the efficiency of our SIZCOR criterion. Of the 93 X-ray–selected clusters in the EMSS sample, 39 (or 41%) have SIZCOR $\geq$ 1.5 and would therefore have been selected by us for more quantitative evaluation. A check of the 39 sources with SIZCOR $\geq$ 1.5 shows that ~70% have redshift $\leq$0.2, while for the 54 clusters with SIZCOR < 1.5 only one-third have redshift $\leq$0.2 (qualitatively consistent with previous statements about decreasing ability to detect X-ray extent as a function of

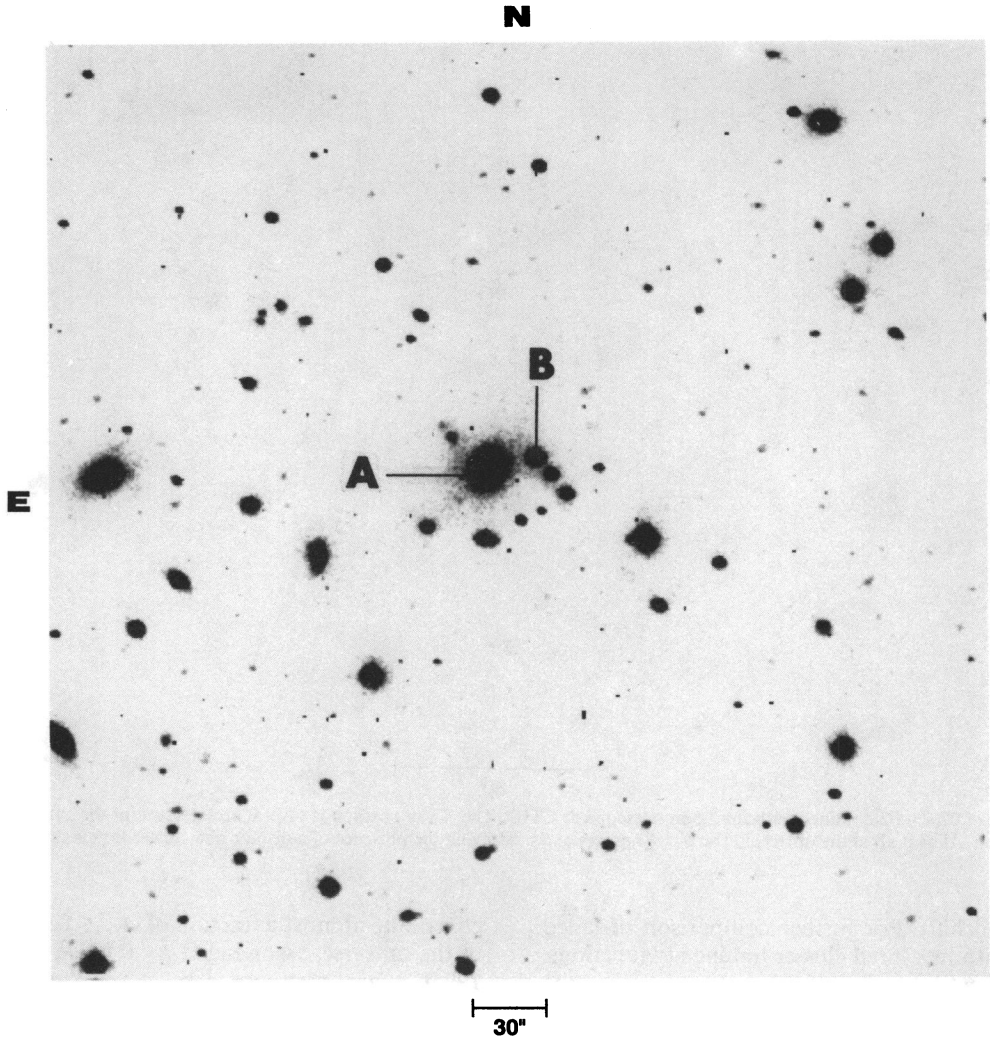

FIG. 6.—*I*-band image of 2307−44 obtained with the 0.9 m telescope at CTIO. Galaxies marked "A" and "B" and the X-ray position are discussed in the text. The majority of objects in the picture are galaxies, indicating the presence of a substantial cluster surrounding "A." The deduced diameter and luminosity of "A" are typical of central, dominant galaxies in clusters.

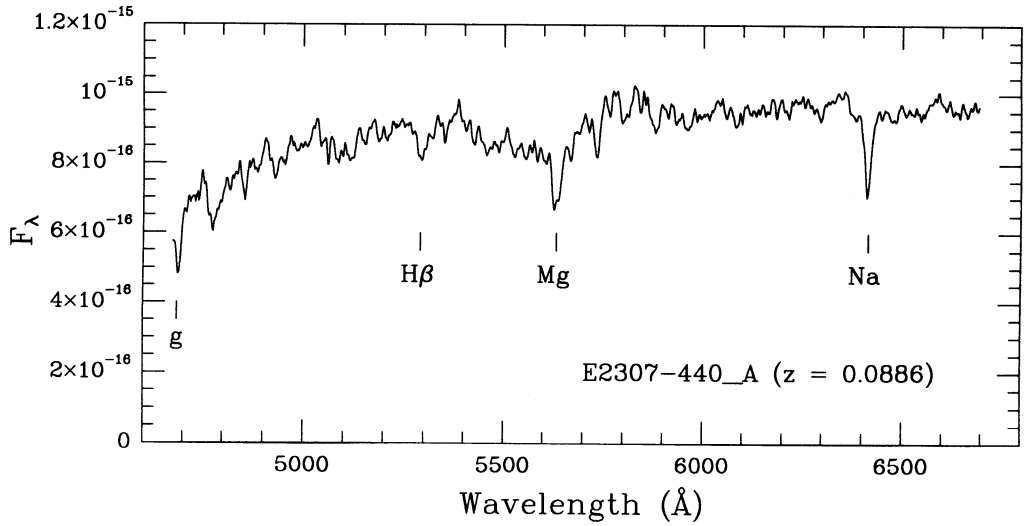

FIG. 7.—Spectrum of Galaxy "A" in the field of 2307−44 obtained with the CTIO 4 m telescope. Redshifted absorption features typical of late type stars indicate a redshift of 0.0886 ± 0.0003. There is no evidence of an active nucleus in this galaxy, as the absorption line at Hβ appears quite normal and there is no sign of an emission line from [O III] λ 5007.

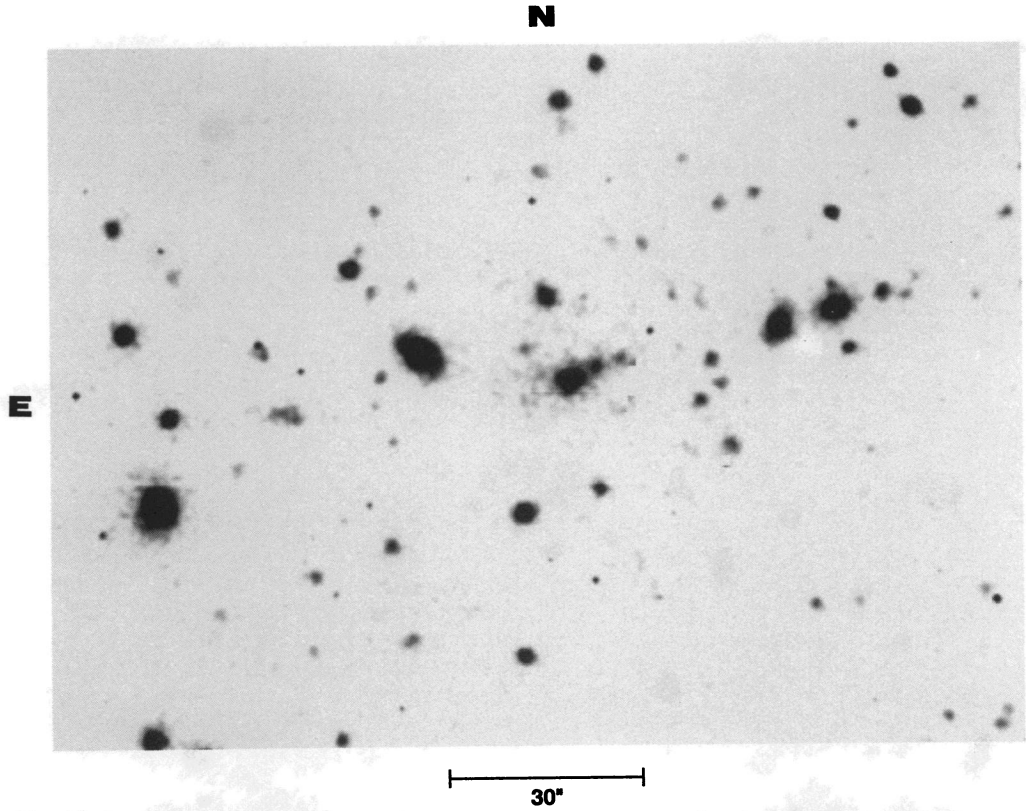

FIG. 8.—*I*-band image of 0207+02 obtained with the 1.5 m telescope at CTIO. The X-ray position is several arcsec south of the galaxy with the extended halo near the center of the figure. Almost all of the objects in the picture are galaxies, implying the presence of a distant rich cluster that is the optical counterpart of the X-ray source.

increasing cluster redshift). For further comparison of failed cluster candidates with measured cluster luminosity functions, we adopt a multiplicative factor of 2.5 to account for the ~40% efficiency of our initial selection process using SIZCOR, thereby raising the upper limit on failed clusters to 15 for comparison with the 93 X-ray–selected clusters in the EMSS. This simple multiplicative factor is tantamount to assuming that failed clusters have similar angular size distributions to X-ray–selected clusters.

Our unsuccessful search strongly suggests that failed clusters are not a significant component of the universe. This is consistent with a hierarchical, bottom-up model for structure formation in which no failed clusters are expected. In the Bootes void, no failed cluster candidates were found in the 27 IPC sequences there which satisfied criteria (1) and (2) of our search strategy. Figure 1 indicates that we could have detected failed clusters with $M_{15} \approx 0.1$ at the distance of the Bootes void. If the characteristic mass distribution of failed clusters is the same as that for the mass distribution of clusters of galaxies (Bahcall & Cen 1993), then the expected number of detections would have been $9\Omega_{fc}$, where Ω_{fc} is the contribution of failed clusters to the overall normalized mass density Ω. The failure to detect any failed clusters implies $\Omega_{fc} < 0.3$ (95% confidence level) in the Bootes void, consistent with the more stringent limits from the *HEAO 1* all-sky survey (Shafer 1983). Thus, any appreciable undetected baryonic matter in the Bootes void cannot be in the form of hot gas clouds for which $\epsilon < 0.01$.

Comparison with the EMSS also sets an interesting limit on the global density of failed clusters. We find that failed clusters are at most one-sixth as common as clusters of galaxies, so they contribute at most a fraction of $\Omega_{fc} \lesssim 0.02$ to the mass density of the universe, assuming $\Omega_{cl} \sim 0.1$ (David, Jones, & Forman 1994). A next step would be to use the *ROSAT* database to refine these results and to investigate whether "inefficient" clusters, that is, ones with $\epsilon \sim 0.01$, exist in significant numbers.

We appreciate the help of a number of our colleagues over the course of this project: C. Stern and C. Jones for the initial analysis of the LMC fields and of a first set of failed cluster candidates; W. Forman for providing the maximum likelihood routine used to establish confidence regions on source extent; D. Worrall and M. Conroy for answering numerous queries concerning IRAF routines and for instructions on how to write an IRAF script; D. Van Stone and J. McDowell for providing a number of unmasked IPC images and updated software essential for our analysis; E. Bohlen for generating optical finding charts and performing ancillary measurements; B. Wilkes and J. Schombert for assistance in evaluating the *IRAS* data; L. Van Speybroeck for providing the data on the *Einstein* mirror performance as a function of angle off-axis; E. Kellogg for guidance with the XPLOT software used to generate figures for the paper; A. Dressler for providing the optical observations indicating a cluster identification for 0657−55; T. Barlow and V. Junkarinen for providing the optical observations indicating a cluster identification for 1703−01; and L. David, J. Hughes, and M. Birkinshaw, for thoughtful comments on initial drafts of this paper. We thank P. Zhao and J. McClintock for providing the images of 2307−44 from which Figure 6 is derived. M. Metzger very kindly obtained the expo-

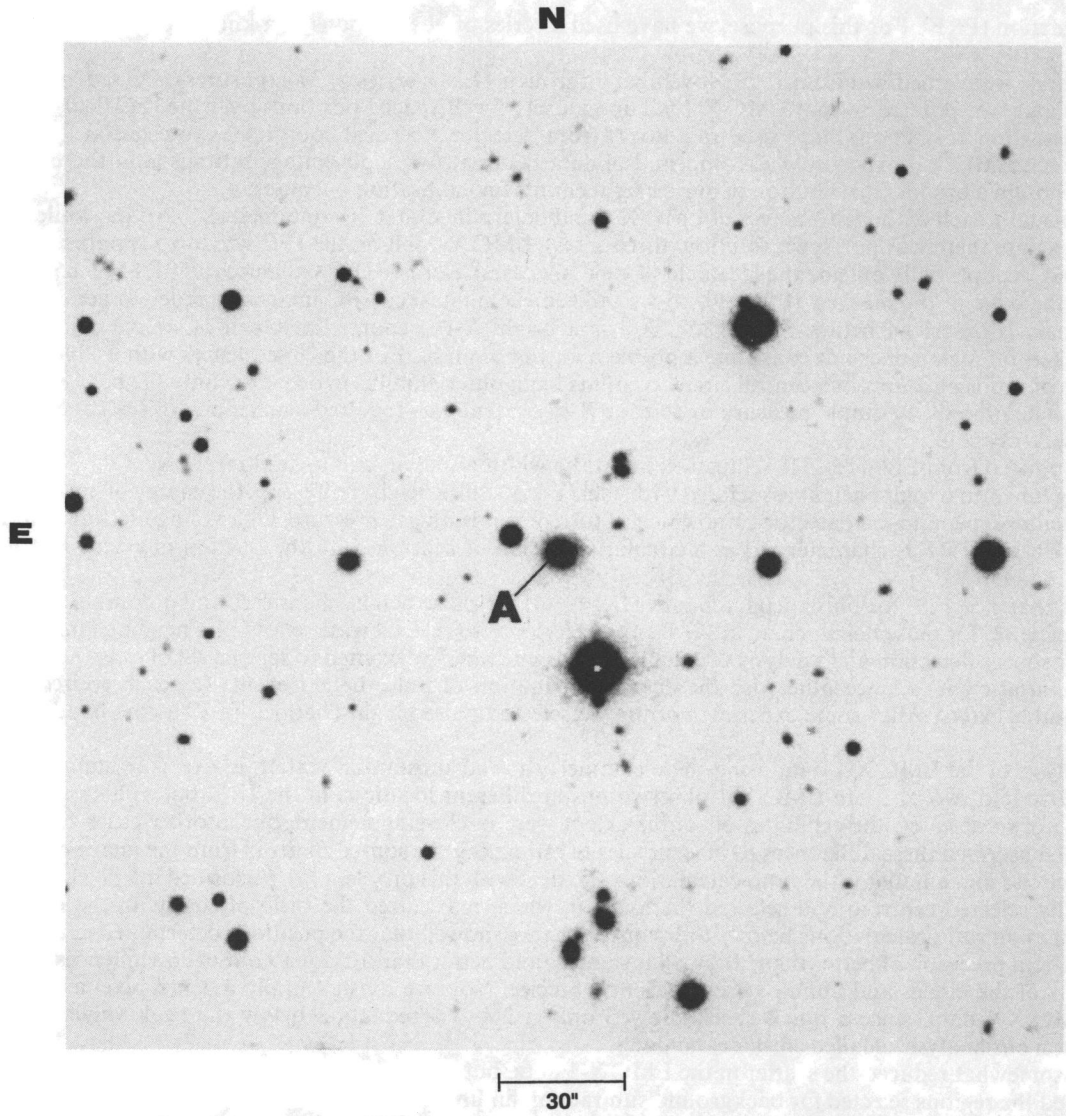

FIG. 9.—*R*-band image of 1615+33 obtained with the 2.4 m telescope at MDM Observatory. The X-ray position is ~30″ NE of the galaxy marked "A," which appears to be the dominant member of a distant, rich cluster. There are at least 39 galaxies within 2′ of galaxy A, with many more faint objects that may well be additional cluster members.

sures for candidate failed cluster fields which we processed to derive Figures 3, 4, 5, and 9. We are grateful to the IPAC Data Center for providing *IRAS* data for a number of the candidate failed clusters and to the *ROSAT* Science Data Center for rapid provision of the processed data for the *ROSAT* observation of 2307−44. The NASA/IPAC Extragalactic Database (NED) operated by the Jet Propulsion Laboratory, CalTech, under contract with NASA, facilitated searches of various catalogs for possible identifications, and the SIMBAD database proved highly useful in literature searches and identifications as well. This work has been supported by NASA contracts NAS 8-30751, NAS 8-39073, and NAG 5-2608.

APPENDIX A

USE OF EINSTEIN IPC OBSERVATIONS OF LMC X-1 TO CHARACTERIZE OFF-AXIS POINT RESPONSE FUNCTION

As described in the text, we have generally used the requirement that SIZCOR $\geq$ 1.5 to select candidate failed clusters. However, in order to assess whether our candidates are actually extended X-ray emitters, we require a more quantitative indicator. Since most of the candidates are located away from the center of the IPC field of view, we need to examine the off-axis system (mirror plus IPC)

point response function (PRF). For this purpose, we have used a series of observations of a known point source, the X-ray binary LMC X-1.

These observations were scheduled from 1979 November 9 through 11 as a series of 37 exposures (IPC seq. numbers 6498–6534). The *Einstein* telescope was pointed so that LMC X-1 fell upon a set of well-spaced positions over the IPC field, in order to develop the "DCOR" (distortion correction) maps used to convert from detector electrical coordinates to celestial location (see H84 for further details). Each LMC X-1 exposure was comprised of data taken at two high-voltage settings (and therefore effectively two gains) in order to obtain a broader distribution of pulse height counts for calibration purposes.

We examined visually each of the IPC images of LMC X-1 and determined that 26 contained usable data, while 11 sequences had to be discarded because there was no aspect solution (three cases), LMC X-1 fell on the IPC window support structure (two cases), or LMC X-1 was at least partially outside the IPC field of view (six cases). For five IPC sequences (6501, 6513, 6519, 6531, and 6532), LMC X-1 fell at the edge of the masked IPC field, so we utilized the unmasked IPC images in order to acquire all of the source counts for the analysis described below. Since LMC X-1 is a bright X-ray source, inclusion of source counts from the higher background, masked-off region does not constitute a problem for our analysis. For the 26 sequences with usable LMC X-1 data, we computed a series of ratios of counts in a central circle to counts in an outer annulus in order to study the behavior of a point source as a function of angle off-axis. A simple measure or test for X-ray extent was required since many of the candidate failed clusters have relatively few X-ray counts.

Figure 10 (reproduced from Fig. 11 of H84) illustrates that the width of the on-axis spatial response of the IPC (plus mirror) is a rapidly decreasing function of pulse height associated with each X-ray. Pulse height represents the energy of an X-ray event, with the actual measured value depending on detector gain, which in turn depends on gas pressure, high voltage setting, and location within the detector. The on-axis PRF is characterized as a circular Gaussian of width σ, with the fraction of events interior to a circle of radius r given by $[1 - e^{-(r^2/2\sigma^2)}]$.

Figure 6 shows that $\sigma \simeq 120''$ for pulse height channel 1, $\sigma \simeq 44''$ for pulse height channel 5, and σ continues to slowly decrease reaching a value of $\simeq 32''$ for pulse height channel 12. Our objective was to select a wide set of pulse height channels to maximize the signal-to-noise for source detection and analysis of extent. At the same time, we wanted to select a set of pulse height channels which saw a minimum variation in σ since otherwise the actual distribution of pulse height events for each source would affect our assessment of possible extent. After some experimentation, we selected pulse height channels 5–12 as the band best meeting these competing criteria.

Our initial analysis of the LMC X-1 data using these channels showed substantial scatter, in excess of statistical uncertainty. In several instances, we had two or more LMC X-1 observations at different locations in the IPC, but at almost identical distances off-axis. For some of these cases, the estimates of source extent were in close agreement, but in other cases significant differences were found. We first ascribed these differences to inaccuracies in estimating the source centroid from the image display and therefore the placement of circles and annuli for the ratio calculations. To deal with this problem, we performed a 5 pixel × 5 pixel raster scan around the visually selected centroid and selected the location which maximized the ratio of counts in the inner circle to outer annulus (see specifics on ratio calculations below). Subsequent checks showed that the positions determined in this way agreed with that for LMC X-1 to a precision of better than 20″ in all instances (and better than 10″ for 19 out of 26 sequences) indicating that the refined placements of the circles and annuli were sufficiently precise. Note we did not apply a 3 × 3 pixel averaging to counting ratios for the LMC X-1 data, since a quick check showed only a 2%–5% reduction below the peak value. Such a change has negligible impact on our analysis of failed cluster candidates.

This approach somewhat reduced the scatter in the LMC X-1 data, but still not to the level expected based on counting statistics. We double-checked the regions selected for background subtraction finding essentially no effect for the bright LMC X-1 source. We determined that the LMC X-1 data were not adversely affected by aspect quality, by breaking up images into subsets with better or poorer aspect quality. We also could find no systematic dependence which related the residual scatter to the average gain associated

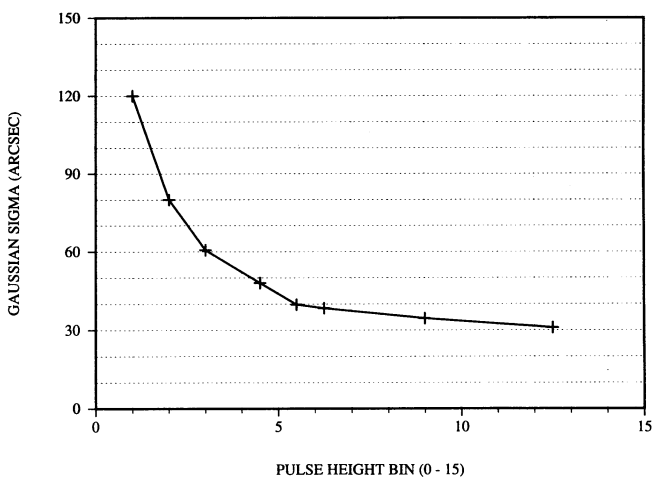

FIG. 10.—On-axis spatial response (σ for Gaussian distribution) for *Einstein* telescope plus IPC as a function of IPC pulse height channel. Crosses correspond to measurements for specific pulse height channels, and the curve is a set of straight line connections between the individual data points.

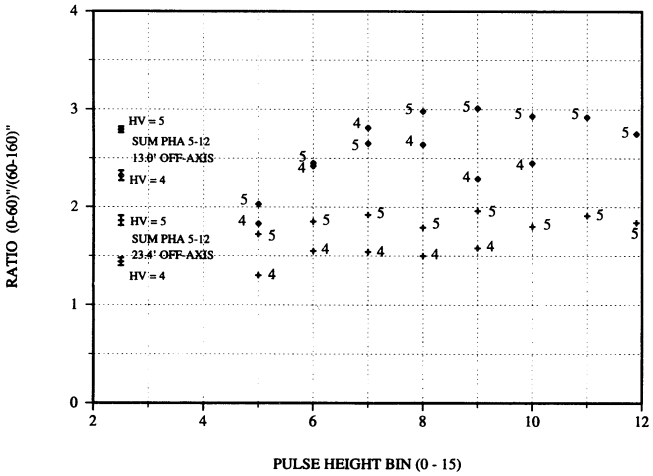

FIG. 11.—Ratio R3 for two different observations of LMC X-1 plotted vs. pulse height channel stepped from 5 to 12. The no. 5 is used to indicate data taken at high voltage step 5 and higher gain than data marked with the no. 4, taken at high voltage step 4. The upper set of 5's and 4's corresponds to IPC seq. 6517, with LMC X-1 13'.0 off-axis and the lower set of 5's and 4's corresponds to seq. 6508, 23'.4 off-axis. Missing 4's correspond to points deleted due to too few observed counts. The data plotted at pulse height bin 2.5 correspond to the sums for pulse height channels 5 through 12, and 1 σ error bars are also shown for these data. Note that R3 depends on HV (and therefore detector gain) for individual pulse height channels and for the sum over channels 5–12.

with the approximate location of LMC X-1 in the IPC for each observation. Finally, we divided the data for each image into separate segments as a function of high voltage setting. (For these LMC X-1 observations, HV = 4 and HV = 5 levels were used.)

After this step, the ratios showed a systematic effect, with each of the 26 observations having a more centrally peaked image for HV = 5 than the HV = 4 data, but the data as a function of angle off-axis still showed excessive scatter. Furthermore, a careful examination of data in a single pulse height channel for a given LMC X-1 location, showed that HV = 4 and HV = 5 observations differed significantly and systematically.

This situation is illustrated by the data in Figure 11 where the ratio of counts from (0–60)″ to the counts from (60–160)″ has been calculated for each individual PHA channel from 5 to 12 for two LMC X-1 observations, seq. 6517 with the source 13'.0 off-axis and seq. 6508 with the source 23'.4 off-axis. Points with fewer than 200 total counts have been deleted from the plot due to poor statistical precision. Error bars on individual points range from ~2% to ~12%. The points plotted at pulse height channel 2.5 are calculated using all of the counts from channels 5 through 12 and the 1 σ error bars for the sums are also shown. On a channel-by-channel basis, the HV = 5 data are more centrally peaked than the HV = 4 data, and of course this result is also apparent in the summed data.

This effect indicates that the PRF does not depend solely on pulse height and distance off-axis, but must also depend on the "local" gain within the IPC. Changing the high voltage setting effectively changes the local gain everywhere in the counter and demonstrates this effect. The key conclusion is that the presence of known (but not fully mapped) local gain variations within the counter (due primarily to imperfect wire spacings) introduces a certain irreducible scatter in the off-axis PRF. In retrospect we note that the local gain controls the charge spreading for each individual X-ray event. Local gain variations will therefore affect the scatter of event locations associated with a given source (which contributes to the width of the PRF).

Working with the LMC X-1 point source, we computed three sets of ratios using net counts within a circle centered on the source and net counts within an adjacent annulus:

counts (0–80)″/counts (80–160)″ = R1
counts (0–60)″/counts (60–120)″ = R2
counts (0–60)″/counts (60–160)″ = R3.

None of these three choices was significantly better than the others in minimizing the scatter for the LMC X-1 data. We also calculated the expected behavior for Gaussian-shaped sources with σ = 0″ (point), 60″, 120″, and 180″. For these calculations, we used an IPC plus mirror Gaussian response width σ = 36″ (characteristic of an on-axis observation and IPC pulse channels 7 and 8, in the midrange of σ for pulse height channels 5–12). The σ for the source was combined in quadrature with the σ for the system

TABLE 2

PREDICTED ON-AXIS COUNTING RATIOS FOR VARIOUS SIZED EXTENDED SOURCES

Source Extent	R1	R2	R3
0'	10.8	3.06	3.01
1'	1.07	0.67	0.50
2'	0.49	0.42	0.24
3'	0.40	0.37	0.20

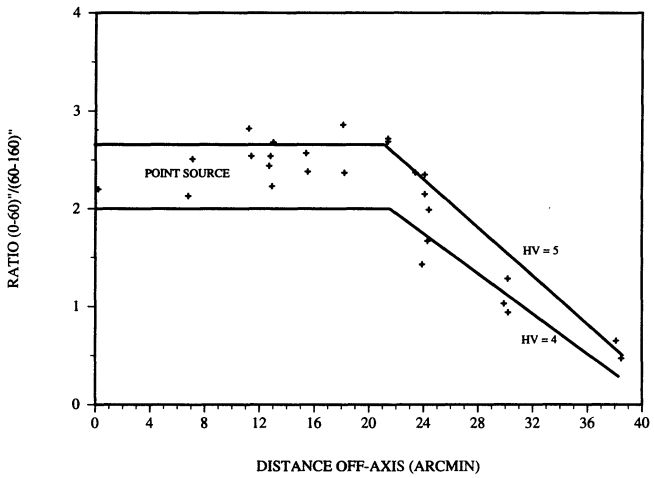

FIG. 12.—Ratio R3 for observations of LMC X-1 as a function of angular distance off-axis. Each individual cross corresponds to a separate LMC X-1 observation with data obtained at both HV 4 and HV 5 summed together. The size of the crosses corresponds approximately to the $\pm 1\ \sigma$ statistical uncertainty. The horizontal line (with a bend) labeled HV = 5 is the best "eyeball" fit to the HV = 5 LMC X-1 data (the curve closely resembles the least squares quadratic fit to the data; see text for details.) The broken line labeled HV = 4 corresponds to the equivalent fit for the HV = 4 LMC X-1 data. For a realistic range of IPC gains, the R3 value for a point source should generally fall between the pair of curves (HV = 5 and HV = 4) as a function of distance off-axis.

response, and the number of source counts in the inner circle and outer annulus, as well as the ratio, were computed for each of the three sets of regions defined above.

Results are summarized in Table 2. The advantage of R3 relative to R2 is apparent from the table in that the ratios are quite similar for point sources while R3 shows significantly more change than R2 as the source becomes extended. Also by collecting events out to 160″ rather than 120″, both R1 and R3 obtain and use a significantly higher fraction of the counts from an extended source than does R2 (e.g., 56% versus 33% for a 120″ source). Our experience with real data indicates that ratios for a weak X-ray source are somewhat more unstable for R1 due to too few counts outside of 80″, while splitting the data at 60″ appears to lead to more "stable" behavior. Therefore, we elect to use R3 for our LMC X-1 calibration and subsequent analysis of failed cluster candidates.

Figure 12 shows the LMC X-1 data as the ratio (R3) of counts from (0–60)″ to counts from (60–160)″ plotted versus angle off-axis (in arcminutes). The crosses show the total LMC X-1 data (HV = 4 plus HV = 5) for each of the 26 observations, with the size of each data point approximately the size of the $\pm 1\ \sigma$ statistical uncertainty. Note the relatively close agreement for some pairs of data points such as those at $\sim 21'$ off-axis, as well as the substantial scatter for the six points at $\sim 24'$ off-axis.

We use the separate HV = 4 and HV = 5 data to bound the effects of having an uncertain gain for any individual location in the detector. For the LMC X-1 data, HV = 4 has a gain of ~11–12 expressed as the value of BAL (mean channel from 0 to 31 for 1.5 keV aluminum X-rays), while HV = 5 has a gain of ~18–19. This range from 11 to 19 in BAL reasonably covers the variations observed during the early months of *Einstein* operations when temporal variations in global gain were significant (and is more than sufficient for later operations when temporal variations were much smaller) as well as the range in gain observed as a function of source location within the detector (see Figs. 4 and 5 of H84). We have calculated linear and quadratic least square fits to the separate HV = 4 and HV = 5 LMC X-1 data, as well as determining the broken line "eyeball" fits shown in Figure 8 (which are quite similar to the quadratic fits, but without a small, probably nonphysical, decrease in the ratio R3 for the central 10′ of the field of view).

As an independent check of these fits, we convolved separate IPC and mirror Gaussian response functions and computed the change in R3 as a function of off-axis angle. The mirror response is much better than the IPC on-axis response so we required the IPC response to fit approximately the midpoint of the on-axis range of R3 values; choosing $\sigma_{IPC} = 39''$ gives a value of R3 = 2.27. For the mirror, we worked at both the best focus for a flat focal surface and for a curved focal plane (better performance) as a function of distance off-axis. With the nominal on-axis focus set several mm behind the IPC window, the typical soft X-ray stops forward of the flat focal plane surface and closer to the curved surface, which may therefore be a more relevant characterization at least out to ~20′ off axis. The mirror Gaussian is essentially negligible (relative to the IPC) out to 10′ off-axis (mirror $\sigma = 5''.4$ for the curved focal plane location, producing an overall σ of 39″.4 and a calculated ratio of R3 = 2.20). However, the mirror Gaussian increases approximately as the square of the angle off-axis and by 20′ the value is 19″.3, producing an overall σ of 43″.5 and a calculated R3 = 1.59; at 30′ off-axis, the mirror σ is 39″.8, the composite σ is 55″.7 and the predicted R3 = 0.81. These numbers are in reasonable qualitative agreement with the behavior illustrated by the pair of broken lines fit to the actual observations in Figure 8, giving us confidence in the validity of our ad hoc technique.

The scatter of the LMC X-1 total data (HV = 4 plus HV = 5) within and occasionally outside of the limiting curves indicates that the curves give a reasonable (but not perfect) definition of the region in which we would expect to find the value of R3 for a point source. An extended source should show R3 falling below the lower (HV = 4) lines, and this is the region of interest for our analysis of candidate failed cluster sources.

REFERENCES

Bahcall, N. A., & Cen, R. 1993, ApJ, 407, L49
Barlow, T., & Junkarinen, V. 1992, private communication
Batuski, D. J., Burns, J. O., Newberry, M. V., Hill, J. M., Deeg, H.-J., Laubscher, B. E., & Elston, R. J. 1991, AJ, 101, 1983
Blumenthal, G. R., Faber, S. M., Primack, J. R., & Rees, M. J. 1984, Nature, 311, 517
David, L. P., Arnaud, K. A., Forman, W., & Jones, C. 1990, ApJ, 356, 32
David, L. P., & Blumenthal, G. R. 1992, ApJ, 389, 510
David, L. P., Forman, W., & Jones, C. 1991, ApJ, 380, 39
David, L. P., Jones, C., & Forman, W. 1994, in Proc. ROSAT Science Symp. Workshop, in press
de Lapparent, V., Geller, M. J., & Huchra, J. P. 1989, ApJ, 343, 1
———. 1991, ApJ, 369, 273
Dressler, A. 1992, private communication
Edge, A. E., & Stewart, G. C. 1991, MNRAS, 252, 428
Einasto, J., Saar, E., Einasto, M., Freudling, W., & Gramman, M. 1994, ApJ, 429, 465
Gioia, I. M., Maccacaro, T., Schild, R. E., Wolter, A., Stocke, J. T., Morris, S. L., & Henry, J. P. 1990, ApJS, 72, 567
Harnden, F. R., Fabricant, D. G., Harris, D. E., & Schwarz, J. 1984, Scientific Specification of the Data Analysis System for the Einstein Observatory (HEAO-2) IPC, Smithsonian Astrophysical Observatory, Special Report 393 (H84)
Harris, D. E., et al. 1993, The Einstein Observatory Catalog of IPC X-ray Source, NASA Publication TM108401
Hasinger, G., Turner, T. J., George, I. M., & Boese, G. 1992, ROSAT PSPC: The On-Axis Point Spread Function: In-flight comparison with the PANTER results, NASA Goddard Space Flight Center, OGIP Calibration Memo CAL/ROS/92-001
Henry, J. P., Gioia, I. M., Maccacaro, T., Morris, S. L., Stocke, J. T., & Wolter, A. 1992, ApJ, 386, 408
Hughes, J. P. 1989, ApJ, 337, 21
Hughes, J. P., Butcher, J. A., Stewart, G. C., & Tanaka, Y. 1993, ApJ, 404, 611
Kang, H., Cen, R., Ostriker, J. P., & Ryu, D. 1994, ApJ, 428, 1
Landolt, A. U. 1992, AJ, 104, 340
Marzke, R. O., Huchra, J. P., & Geller, M. J. 1994, ApJ, 428, 43
Moody, J. W., Kirshner, R. P., MacAlpine, G. M., & Gregory, S. A. 1987, ApJ, 314, L33
Peebles, P. 1980 The Large Scale Structure of the Universe (Princeton: Princeton Univ. Press)
Puchnarewicz, E. M., et al. 1992, MNRAS, 256, 589
Rees, M. J., & Ostriker, J. P. 1977, MNRAS, 179, 541
Shafer, R. 1983, Ph.D. thesis, Univ. Maryland
Silk, J. 1977, ApJ, 211, 638
Stocke, J. T., Morris, S. L., Gioia, I. M., Maccacaro, T., Schild, R., Wolter, A., Fleming, T. A., & Henry, J. P. 1991, ApJS, 76, 813
Tsuru, T. 1991, Ph.D. thesis, Univ. Tokyo
Tucker, W. H., et al. 1994, in preparation
White, S. D., & Frenk, C. S. 1991, ApJ, 379, 52
White, S. 1991, in Clusters and Superclusters of Galaxies, ed. A. Fabian (Dordrecht: Kluwer), 17